Solar Physics (2005) 230: 169–204

THE SPECTRAL IRRADIANCE MONITOR: MEASUREMENT EQUATIONS AND CALIBRATION

JERALD W. HARDER, JUAN FONTENLA, GEORGE LAWRENCE, THOMAS WOODS and GARY ROTTMAN
Laboratory for Atmospheric and Space Physics, University of Colorado, Boulder, Colorado 80309, U.S.A.
(e-mail: jerald.harder@lasp.colorado.edu)

(Received 6 April 2005; accepted 28 July 2005)

Abstract. The Spectral Irradiance Monitor (SIM) is a satellite-borne spectrometer aboard the Solar Radiation and Climate Experiment (SORCE) that measures solar irradiance between 200 and 2700 nm. This instrument employs a Fèry prism as a dispersing element, an electrical substitution radiometer (ESR) as the primary detector, and four additional photodiode detectors for spectral scanning. Assembling unit level calibrations of critical components and expressing the sensitivity in terms of interrelated measurement equations supplies the instrument's radiant response. The calibration and analysis of the spectrometer's dispersive and transmissive properties, light aperture metrology, and detector characteristics provide the basis for these measurement equations. The values of critical calibration parameters, such as prism and detector response degradation, are re-measured throughout the mission to correct the ground-based calibration.

1. Introduction

The Spectral Irradiance Monitor (SIM) is a satellite-borne spectrometer aboard the Solar Radiation and Climate Experiment (SORCE) that measures solar spectral irradiance between 200 and 2700 nm. This paper is a companion paper to Harder *et al*. (2005) that appears in this same issue of *Solar Physics*. That paper describes the overall instrument requirements, the hardware implementation, and the measurement modes needed to acquire the scientific data. This current paper emphasizes the calibration methods, in-flight corrections, and the mathematical operations (measurement equations) that are needed to convert instrument hardware signals measured in engineering units into SI units (International System of Units) of spectral irradiance with units of Wm^{-3}, or equivalently $\mathrm{Wm}^{-2}\,\mathrm{nm}^{-1}$ (Parr, 1996). Section 5 of this paper give the status of the calibration, and the corrections that have been included up to this point in time that are not covered by the measurement equations discussed in this paper.

Briefly summarizing Harder *et al.* (2005), SIM implements a number of unique design characteristics to provide: (1) broad wavelength operation, (2) multiple focal plane detectors, (3) a very high precision wavelength drive, and (4) in-flight monitoring of instrument response degradation. The instrument uses a low light scattering Fèry prism as the dispersing element that has high optical throughput

within the 210–2700 nm region with a variable resolving power ($\lambda/\Delta\lambda$) ranging from 400 at 250 nm to a minimum of 33 at 1200 nm. The prism has excellent imaging properties, so multiple detectors can be used to detect incoming light in the instrument's focal plane. The primary detector is an electrical substitution radiometer (ESR). The ESR is a thermal detector that measures light from the spectrometer using phase sensitive detection to dramatically reduce the effect of thermal drift and detector noise. The input light beam to the spectrometer is chopped at 0.01 Hz by a shutter and only signal variations at the fundamental frequency are used to determine radiant power. The ESR detector calibrates the radiant sensitivity of four photodiode detectors during flight. The most important in-flight irradiance correction factor is prism transmission degradation, so the instrument is designed as two back-to-back, mirror image spectrometers that are coupled with a periscope. This provides both direct measurement of prism transmission and end-to-end comparisons by the two independent instruments. The two spectrometer configuration also provides instrument redundancy to ensure the continuity of the data record if the working spectrometer should fail.

The operation of the SIM radiometer is schematically represented in Figure 1. Solar radiation, E_λ (units of Wm^{-2}), is incident on the instrument's rectangular entrance slit of area A (units of m^2); it is the limiting aperture that defines the total radiant power entering the spectrometer. The light is then dispersed by the prism and imaged on an exit slit. The prism's geometry, orientation, and index of refraction, along with the entrance and exit slit widths, determine the selected wavelength (λ_s) and spectral bandpass ($\Delta\lambda$) that is transmitted through the exit slit and impinges on the detectors. This slit function convolution is effectively a low-pass filter of the spectrally complex solar spectrum over the wavelength band $\Delta\lambda$. A photometric detector, either the ESR or a photodiode, measures the incident power, P_D, within the spectral bandpass. The measured spectral irradiance, $\mathcal{E}_\lambda(\lambda_s)$ (units of $\mathrm{Wm}^{-2}\,\mathrm{nm}^{-1}$), is then derived from three components: the determination

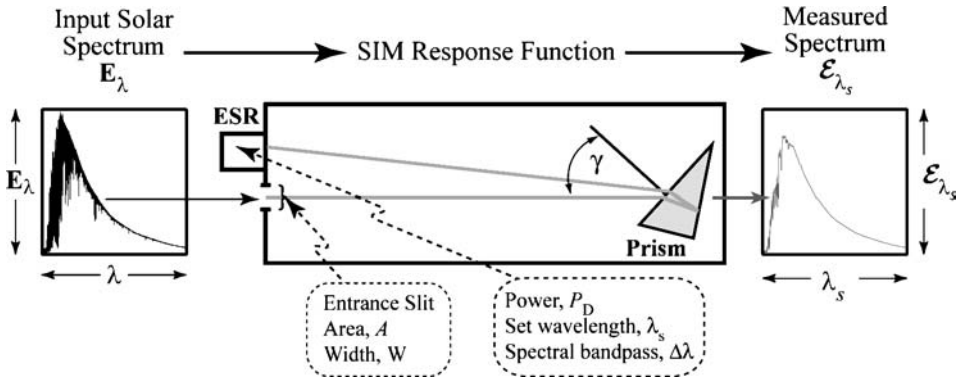

Figure 1. The figure schematically shows the spectrometer's response function and the detection of radiant power by a detector (ESR) in the instrument's focal plane.

of the instrument bandpass by the process of slit function convolution, calibration of the slit area, and the determination of radiant power by the detector:

$$\mathcal{E}_\lambda(\lambda_s) = \frac{P_D(\lambda_s)}{A\Delta\lambda} \quad (\mathrm{Wm^{-2}\,nm^{-1}}). \tag{1}$$

This simplified picture neglects numerous important corrections, like the orbital parameters solar distance and the Doppler effect, and wavelength-dependent corrections like prism aberrations and transmission, detector efficiency and temperature effects, diffraction, and time-dependent degradation processes. The term $A\Delta\lambda$ is, in reality, an integral over these wavelength-dependent contributions.

The block diagram in Figure 2 shows the unit level calibrations needed to measure spectral irradiance and their associated measurement equations. The calibration parameter table lists the methods used to derive their value and marks (*) the calibrations that require in-flight modification. In addition, the rounded rectangles show where these in-flight corrections are inserted into the measurement process.

The wavelength calculation equations convert prism encoder positions into wavelength information. This set of equations gives the relationships between target wavelength (λ_s), the charge coupled device (CCD) encoder reading (C), and the spectral focal plane coordinate, (y_s). Section 2 describes the dispersion geometry, and the detailed transformations between these variables are presented in Appendix A. In Section 3, a number of instrument characteristics, calibrations, and in-flight corrections are combined to give the spectral instrument profile, $\mathbf{S}(y_s)$, describing the wavelength-dependent radiometric response of the instrument. In addition, the instrument function, $S'(\lambda_s, \lambda)$, described in Section 3.1 gives the function needed to convolve other higher resolution data to the resolution of SIM. This is important for comparing other tabulated or modeled solar spectra against the measured SIM irradiance, it is also used for interpreting laboratory spectra from atomic lamps and other wavelength standards such as Schott Glass BG20 filters. Section 4 describes the methods used to determine the radiant power detected by the SIM focal plane detectors. The ESR is the absolute detector for this instrument, and phase sensitive power detection is used to minimize the effects of $1/f$ noise inherent in thermal detectors. Four photodiode detectors complement the ESR to produce low-noise, fast response spectral scans. This operational mode produces the most useful information about the time series of solar spectral variability (see Rottman *et al.*, 2005). However, the ESR continually recalibrates the in-flight photodiode detectors (Section 4.2).

2. Prism Dispersion

The set of equations needed to define the focal plane coordinate system starts with the dispersion geometry of a prism in Littrow configuration and is derived from

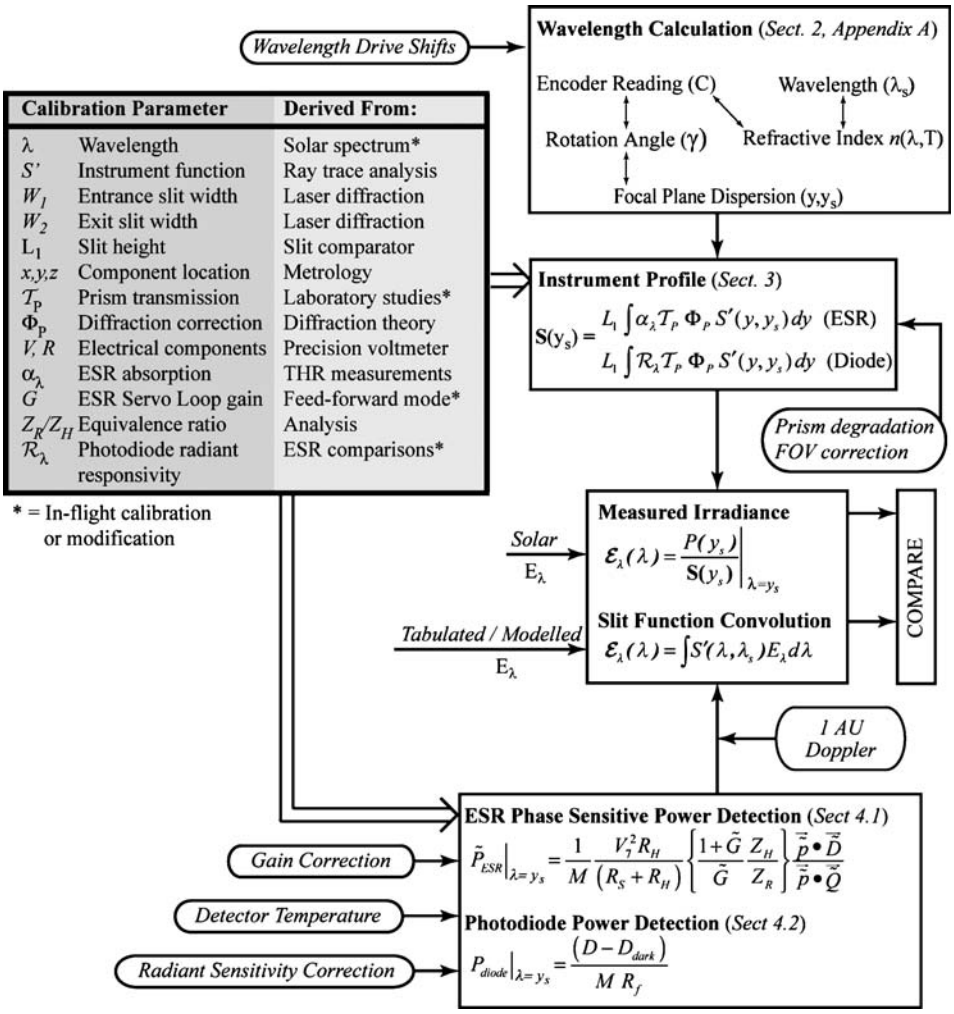

Figure 2. The SIM measurement equations used to calculate solar spectral irradiance in block diagram form. Processes shown in *square blocks* are equations and actions specific to the SIM instrument and the sections discussing these equations are noted along with the title of the block. Calibration quantities needed for these equations are identified and listed in the *gray box*. In-flight correction factors are shown as *rounded rectangles* and where they are inserted in the measurement process.

Snell's law for a plane surface prism:

$$2\theta_{\mathrm{P}} = \sin^{-1}\left(\frac{\sin(\gamma)}{n}\right) + \sin^{-1}\left(\frac{\sin(\gamma-\phi)}{n}\right). \tag{2}$$

The dispersion geometry and the definitions of the symbols in Equation (2) are shown in Figure 3. Equation (2) and Figure 3 in this paper are the same as Equation

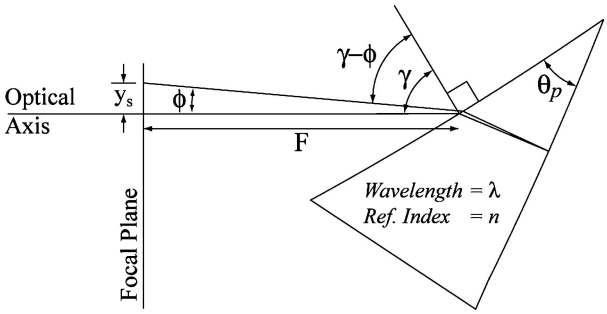

Figure 3. The dispersion geometry of the Fèry prism and the definitions of the variables described in Equation (2) and Appendix A.

(3) and Figure 8 of Harder *et al.* (2005). In this first paper, they are used to describe the dispersion properties of the instrument, and here they are the starting point for developing the analytical equations for the wavelength calculation.

In Figure 3, γ is the prism rotation angle derived from the CCD encoder position C; the refraction angle, ϕ, or its equivalent focal plane coordinate y is found from the prism rotation angle and wavelength of incident light; the index of refraction n is a unique surrogate for wavelength, λ, and is derived from the rotation angle and geometry of the prism. The analytical equations associated with these transformations are presented in four separate sections in Appendix A, and these analytical results are verified through ray tracing. While there are several equations to relate the wavelength scale to the prism angles and the focal plane CCD encoder system, it is important to note that the SIM wavelength scale is a deterministic process. Slight offsets and stretches during flight are corrected against a SIM-measured reference spectrum that is then used to adjust all other spectra. This single reference spectrum is then calibrated by comparison with a higher resolution solar spectrum convolved with the SIM instrument function. At the present time, the Thuillier *et al.* (2003) Composite 1 spectrum is used for this process. It should be noted that since 21 April 2004, no measured spectra have been shifted relative to this reference. The shift-stretch algorithm is used to correct data prior to that date, which have been affected by an operational problem related to the action of the prism drive system; see Section 5 for further discussion.

3. Instrument Function Convolution

The theoretical SIM instrument function $s(\lambda_s, \lambda)$ can be found by convolving identical entrance and exit slit rectangular functions of width W in the focal plane coordinate system to yield a triangular function with an area of W. Division by the focal plane dispersion $(\partial y/\partial n)(\partial n/\partial \lambda)$ converts it into the equivalent wavelength coordinates. The instrument function acts as a convolution kernel with unit

area:

$$\int s\,(\lambda_s, \lambda)\,\mathrm{d}\lambda = 1. \tag{3}$$

When an external reference solar spectrum is convolved with $s(\lambda_s, \lambda)$ a spectrum is produced at the SIM resolution with the property that the integrals of $\mathbf{E}_\lambda(\lambda)$ and $\mathcal{E}_\lambda\,(\lambda_s)$ have the same area:

$$\mathcal{E}_\lambda\,(\lambda_s) = \int s\,(\lambda_s, \lambda)\;E_\lambda\,(\lambda)\;\mathrm{d}\lambda \quad \text{such that} \quad \int E_\lambda\,(\lambda)\;\mathrm{d}\lambda = \int \mathcal{E}_\lambda\,(\lambda_s)\;\mathrm{d}\lambda_s. \tag{4}$$

In practice, the function $s(\lambda_s, \lambda)$ presented in Equation (3) is inadequate to describe the actual instrument function. Additional wavelength-dependent corrections must be included within the integral that influence the overall shape of the spectral response function. The response function, represented by $\mathbf{S}(y_s)$ in Figure 2, includes corrections for spectrometer aberrations (S'), prism transmission ($\mathcal{T}_P$), diffraction loss (Φ_P), and ESR and photodiode responsivities R_λ and α_λ. All of these correction factors are smooth functions of wavelength with the exception of α_λ for the photodiode detectors that vary rapidly in the vicinity of the long wavelength cut-off, and the silicon photodiodes have additional structure in the UV part of the spectrum. The correction factors are described in the next four sections except for α_λ, which is discussed in the context of the instrument detectors in Section 4.2.

3.1. $S'\,(\lambda_s, \lambda)$: Instrument function convolution from ray tracing

A ray trace model based on the measured geometry of the prism and locations of the exit slits relative to the entrance slit is used to generate the instrument function, $S'\,(\lambda_s, \lambda)$, to account for optical aberrations and vignetting. Section 2.3.2 of Harder *et al.* (2005) describes the instrument's optical properties in detail but can be summarized here: (1) the predominant aberrations are image magnification and coma, (2) imperfect prism focusing causes some light loss at the exit slit, and (3) prism glass dispersion is a non-linear function of wavelength so the ideal trapezoidal instrument function is slightly asymmetric in wavelength space. All of these optical processes are modeled by ray tracing the spectrometer using both ZEMAX (Focus Software Inc., Bellevue, WA) and IRT (Parsec Technologies, Boulder, CO) software packages. For each of the five SIM detectors, the ray trace computes instrument functions on an index of refraction grid, giving roughly constant spacing in dispersion. The optimizer in the ray trace software determines the rotation angle for each wavelength (λ_s) so that the chief ray hits the center point of the detector exit slit. The rotation angle is then fixed and separate ray traces are performed for ± 100 wavelengths incrementally offset from λ_s. A total of 40 000 randomly distributed rays from an object forming a 0.5° beam pass through the entrance slit and are propagated through the optical system to the focal plane where a mask

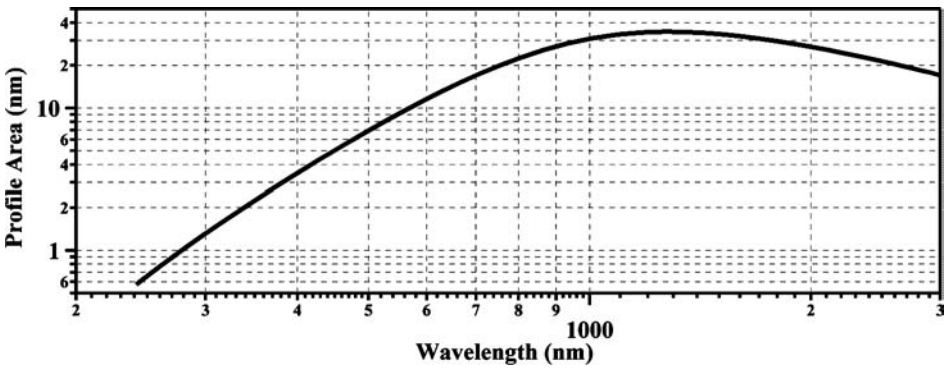

Figure 4. The profile integral over its usable wavelength band as a function of wavelength. The graph is shown on a log–log scale for the ESR detector.

with the dimensions of the exit slit is used to count the number of rays that pass it. As the wavelength shifts away from λ_s by $\delta\lambda$, a smaller fraction of rays pass through the mask. For each λ_s and $\delta\lambda$, the ratio of the number of rays collected at the exit slit to those passing through the entrance slit provides an estimate of the spectrograph's efficiency, $S'(\lambda_s, \lambda)$. One hundred separate instrument functions are generated over each detector's usable wavelength range. The profile integral (or equivalent bandwidth) is representative of the spectral bandpass, and is shown in Figure 4 versus wavelength for the ESR detector over its usable wavelength range.

This process generates the proper instrument function for processing spectral irradiances. The reciprocal process that fixes the wavelength and rotates the prism gives a nearly identical result that can be compared to an experiment in which an intense laser line is scanned so the character of the instrument can be seen in the far wings of the instrument function. Figure 5 compares the ray traced SIM slit profile with the scan of a 543.5 nm HeNe laser as measured by the Vis1 photodiode. Other scans of this kind were performed at other wavelengths using discrete laser lines and with a mercury electroless discharge lamp (EDL) and for each detector, but the data shown in Figure 5 displays the best SNR attained for this kind of measurement. The measured out-of-band stray light contribution is about 50 parts per million of the main signal, so does not contribute to the shape of the profile shown in Figure 5. The measured and ray traced profiles qualitatively agree in the core of the trapezoidal function and deviations occur at the 0.5 – 0.01% level. These differences arise from a combination of diffraction and edge scatter generated by the exit slits and baffles. The ratio of the areas of the laboratory calibration to the ray trace profile in this case is 1.0045, indicating that ray traced instrument function adequately describes the instrument function with the exception of small corrections needed for diffraction. Saunders and Shumaker (1986) used a prism and a grating in a double spectrometer configuration to perform a similar experiment, and their findings are in accord with the results for SIM. However, a number of improvements in the comparison must be made before this kind of experiment is deemed a calibration: in particular,

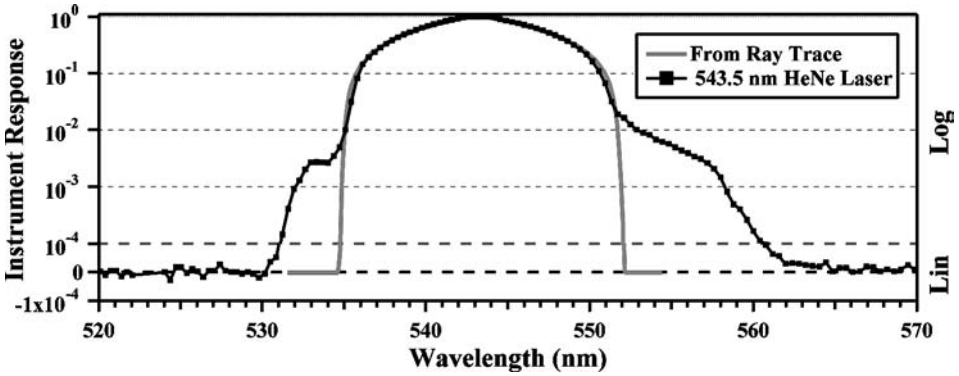

Figure 5. A comparison of instrument function ray tracing with the measurement of a 543.5 nm HeNe laser for the Vis1 photodiode. The graph is a combined log–linear plot with 4 orders of magnitude of response on a log scale and a linear scale below 10^{-4} to show the noise level of the measurement and the zero points of the ray traced trapezoid. The instrument responds to additional sources of light scattering and diffraction in the far wings of the trapezoidal instrument function.

the optical performance of the Fèry prism is strongly f/number-dependent so the input laser beam must fill the spectrometer in the same manner as the Sun (i.e., 0.5° beam) and the emergent flux from the light source must be known so light losses are properly accounted for in the calibration. With the development of the NIST SIRCUS facility (National Institute of Science and Technology, Spectral Irradiance and Radiance Calibrations with Uniform Sources; Brown, Eppaldauer, and Lykke, 2000) calibrations meeting these requirements will be possible for future missions.

3.2. *A*, *W*, *L*: MEASUREMENT OF SLIT DIMENSIONS

An accurate measurement of the entrance slit area is needed to establish the radiant flux into the instrument, and the width of the entrance slit is needed for the determination of the instrument's bandpass and diffraction correction (see Section 3.4). The requirement was set so that its accuracy was commensurate with the accuracy of ESR power measurements, the ability to measure the instrument profile, and the magnitude of the diffraction correction that varies by an order of magnitude over the wavelength span of the instrument. The level of accuracy required for the slit dimension measurements is on the order of 100 –500 ppm):

$$\left(\frac{\delta W_1}{W_1}\right)^2 + \left(\frac{\delta L_1}{L_1}\right)^2 = \left(\frac{\delta A_1}{A_1}\right)^2 \approx (5 \times 10^{-4})^2. \tag{5}$$

Thus, the 0.3 mm slit width must be determined to about $\pm 0.1\ \mu$m accuracy, and the 7 mm tall slit to about $\pm 2.5\ \mu$m. This same specification applies to the exit slits as well.

The slits used for SIM are copper/nickel bimetal etched slits (manufactured by Buckbee-Mears, Inc., Minneapolis, MN) that have a width tolerance of $\pm 8\ \mu$m, and a parallelism of $\pm 4\ \mu$m over the slit's 7 mm length. The bimetal etching process creates an edge with only a few microns in thickness thereby minimizing additional light scattering. Analysis of the slits by scanning electron microscopy indicates there is about 0.3 μm root mean square (RMS) roughness along the slit edge and corner-rounding is about 3 μm in radius. Because of this, slit calibrations are performed to measure the area and the effective width over its entire length. The slit length is then inferred from these two measurements. The width is measured by laser diffraction, and area is measured by comparing the light flux through the slit relative to the light flux through a known, calibrated aperture. These two methods are described in Appendix B.1 and B.2, respectively.

The practice of high-accuracy measurements of long, narrow spectrometer slits is not as advanced as the circular aperture area measurements used for TSI studies (Fowler, Saunders, and Parr, 2000), so the absolute calibration of the two methods described in Appendix B rely on known standard widths and areas. The slit width standard (Photo Sciences Inc., Torrance, CA) is a chrome-on-glass slit measured with a Nikon 2i metrological microscope with a quoted uncertainty of $\pm 0.5\ \mu$m traceable to NIST standards, and the precision of the diffraction calibration method is $\pm 0.03\ \mu$m based on multiple measurements of the slits. The flux comparator system for slit area measurements is based on a standard, 0.5 cm^2, NIST calibrated circular aperture with an area known to $\pm 3 \times 10^{-5}$ mm^2. The apparatus used to measure the area has a precision of $\pm 2 \times 10^{-5}$ mm^2. The uncertainties in the area and width measurements are comparable to the requirement limits of Equation (5), but the standard apertures are retained as a ground witness for recalibration so future improvements in the measurement methods will translate into a refined value for the flight slits.

Since the area and width of the instrument's entrance slit is a function of temperature, appropriate thermal corrections are applied to the flight data. Since the slits are fabricated from a bimetal material, the temperature coefficient of expansion has to be calculated for the bimetal combination (Gere and Timoshenko, 1990) and has a numerical value of 1.58×10^{-5} K^{-1}. The temperature of the slit is monitored in-flight with a thermistor bonded to the nearby UV photodiode.

3.3. $\mathcal{T}_P$: PRISM TRANSMISSION AND DEGRADATION

The calibration of prism transmission and monitoring the degradation of this transmission represent two of the most important activities for the SIM calibration. Prism transmission measurements are discussed in Section 3.3.1 and Appendix C, and the prism degradation model is explained in Section 3.3.2. The measurement of prism transmission is a very difficult and time consuming process, so the actual calibration was performed on two ground witness prisms rather than the actual flight units.

However, these ground witnesses were made from the same boule of Suprasil 300, and were manufactured and aluminized simultaneously with the flight prisms.

3.3.1. *Prism Transmission Measurements*

The transmission of the SIM prism results from a number of sources that are a function of incidence angle and wavelength, and the transmission must be calculated for each of the instrument's detectors since the geometry is different for each of them. Fresnel reflections on the vacuum–glass and glass–vacuum interfaces of the prism cause a loss in transmission that is a function of incidence angle and the index of refraction of the glass for a given wavelength; the intensity of the reflection is also a function of the incoming light beam polarization. Furthermore, this effect is enhanced because the prism rotation angle, γ, is $59^\circ \pm 2.5^\circ$, which is near the Brewster angle for fused silica. Light intensity losses in the bulk of the Si_xO_y glass matrix are significant only in the ultraviolet (UV) for $\lambda < 300$ nm, and in the infrared (IR) for $\lambda > 2700$ nm. Suprasil 300 fused silica glass (Hereaus Amersil Inc., Duluth, GA) is a 'dry glass' with a very low OH content ([OH] $<$ 1 ppm), so the broad and deep hydroxyl absorption features are suppressed in the transmission spectrum (Humbach *et al.*, 1996). This glass is made by a chemical vapor deposit process, so the trace metals that give rise to color centers are present only at the part per billion level, and cannot contribute to the bulk absorption over the effective 24 mm path through the prism. The reflectivity of the aluminized rear-surface of the prism is a function of wavelength, particularly in the 700–900 nm region. Inspection of Figure 3 shows that the light path through the prism is nearly normal to the back surface regardless of rotation angle and wavelength, so there is no polarization effect in the aluminum reflectivity. Laboratory measurements of prism transmission suggest that the reflectivity of the second-surface aluminum mirror on the prism is different from the reflectivity of bare aluminum. Therefore, the combined absorption of the bulk glass and reflectivity of the surface glass–aluminum layer is explicitly measured.

Figure 6 shows the effective mirror reflectivity as measured by the method described in Appendix C. This figure also shows the Fresnel horizontal and vertical two-reflection contributions for the geometry corresponding to the ESR detector; the Fresnel contributions are different for the other detector locations in SIM but can be computed from Equations (C.2) and (C.3) presented in Appendix C. The prism transmission for unpolarized light is the product of an angular-dependent portion arising from the average of the two Fresnel reflections and the measured mirror reflectivity that includes bulk losses in the UV and IR. This formulation has the advantage that the transmission can be computed for all detector positions and all prism rotation angles. The attenuation for wavelengths longer than 2600 nm shown in Figure 6 is caused by absorption in the bulk of fused silica (Humbach *et al.*, 1996). The estimated photometric error from the transmission measurement in the 200–1000 nm is about 0.1%, but in the 1000–2900 nm region the error increases to about 1%.

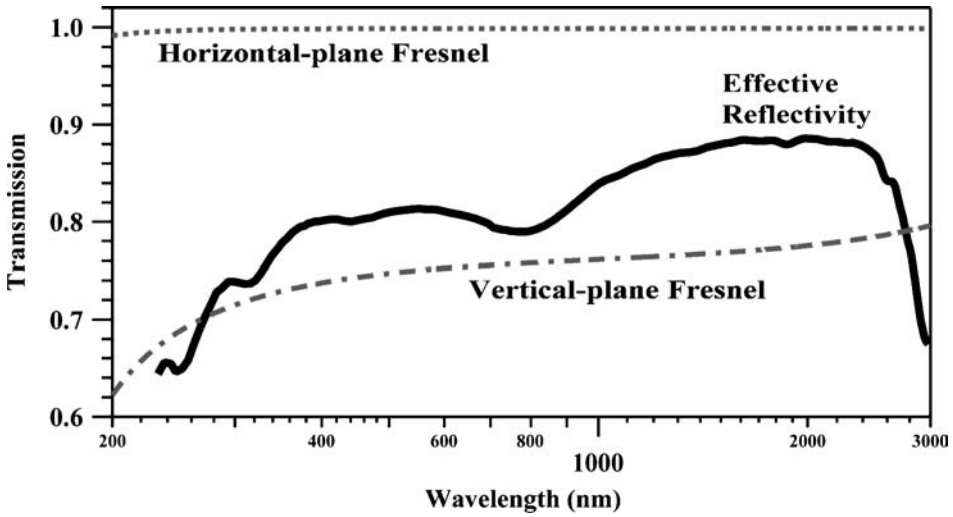

Figure 6. The measured prism transmission. The figure shows the second-surface effective reflectivity of the prism and the two-reflection Fresnel contributions in each polarization. The calibration was done for the geometry of the ESR detector. Transmission for unpolarized light is the product of the reflectivity and the average of the two Fresnel components.

3.3.2. *Prism Degradation Measurement and Model*

Exposure to the space environment causes irreversible changes to the transmissive properties of the prism that must be tracked both as a function of wavelength and time. Complete understanding of the degration characteristics is an ongoing task during the instrument lifetime. This section discusses the in-flight methods that were designed and operate to measure the degradation and the current model applied to determine and correct the degradation observed so far.

Table I summarizes the operation modes used to determine the prism degradation properties, the action of the modes, and the number of days between calibrations. The two primary modes for this purpose are the direct prism transmission calibration mode and the ESR full scan. The SIM A/SIM B comparison is not currently used in the calculation of the prism degradation, but is used as an end-to-end check to ensure that the degradation correction factors are consistent.

Without loss of generality, the prism degradation can be expressed by the equation

$$T(t, \lambda) = T_0(\lambda)\, \mathrm{e}^{-\tau(t,\lambda)}, \tag{6}$$

where τ represents this degradation in a logarithmic scale and is defined as 0 at the beginning of the mission, and T_0 is the un-degraded prism transmission. By using the in-flight measurements, the prism degradation observed until the present can be described by a model that corresponds to the following equation:

$$\tau(t, \lambda) = \kappa(\lambda) C(t). \tag{7}$$

TABLE I
SIM operation modes used to determine prism degradation.

Calibration mode	Action/purpose	Cadence (number/days)
Prism transmission (mode 1)	Uses the SIM ESR prism transmission measurement mode described in Section 2.3.4 of Harder *et al.* (2005). Performs this operation at 44 discrete wavelengths.	1/7
ESR full scan (mode 2)	Measures the solar spectrum over the operating range of the ESR (256–2700 nm) with a sampling of 3 prism steps per resolution element. The range for prism calibrations using the ESR is 300–1100 nm, and the UV photodiode is used for the 210–300 nm region.	1/90
SIM A/SIM B comparison (mode 3)	Simultaneous full scans with SIM A and SIM B provide comparisons and an end-to-end measure of the effectiveness of the degradation corrections.	1/30

With the wavelength and temporal variations accounted for by two separate functions, the absorption coefficient $\kappa(\lambda)$ and the column density $C(t)$, respectively. The function κ is obtained by comparing ESR full scans (mode 2 in Table I), at widely separated times. To date, all of the ESR full scans have been used to check the validity of Equation (7), and this relationship is applicable to within the limitations of observation noise and solar variability. The value of κ will be improved by continued analysis of ESR full scans and the SIM A/B comparisons (mode 3 of Table I). Figure 7a shows this absorption coefficient as a function of wavelength, and shows that absorption is greatest in the near UV, and drops to values indistinguishable from noise by 700 nm thereby indicating that no prism degradation is observed at these longer wavelengths.

The column value shown in Figure 7b is found from the in-flight prism transmission measurement performed on a weekly cadence. Since SIM B receives only 18% of the solar exposure of SIM A, this experiment is done symmetrically so the effects of exposure time on degradation can be assessed. These activities are performed with the hard radiation traps (HRT, see Harder *et al.*, 2005 for details) inserted in the light beam to minimize unnecessary exposure to the prisms. The transmission calibration system yields a relative change in transmission rather than an absolute value. Additional reflections in the calibrator's relay optics (prism, periscope, folding mirror, focusing beamsplitter) alter the polarization state and modify the wavelength dependence of the input light beam so the prism transmission measured through this system has additional contributions not present in the transmission function measured by the ground calibration system and described in Section 3.3.1. However, the modifications induced by the relay optics are believed to be time invariant since light flux on these elements is very small and these optical elements are common to both the I and I_0 modes.

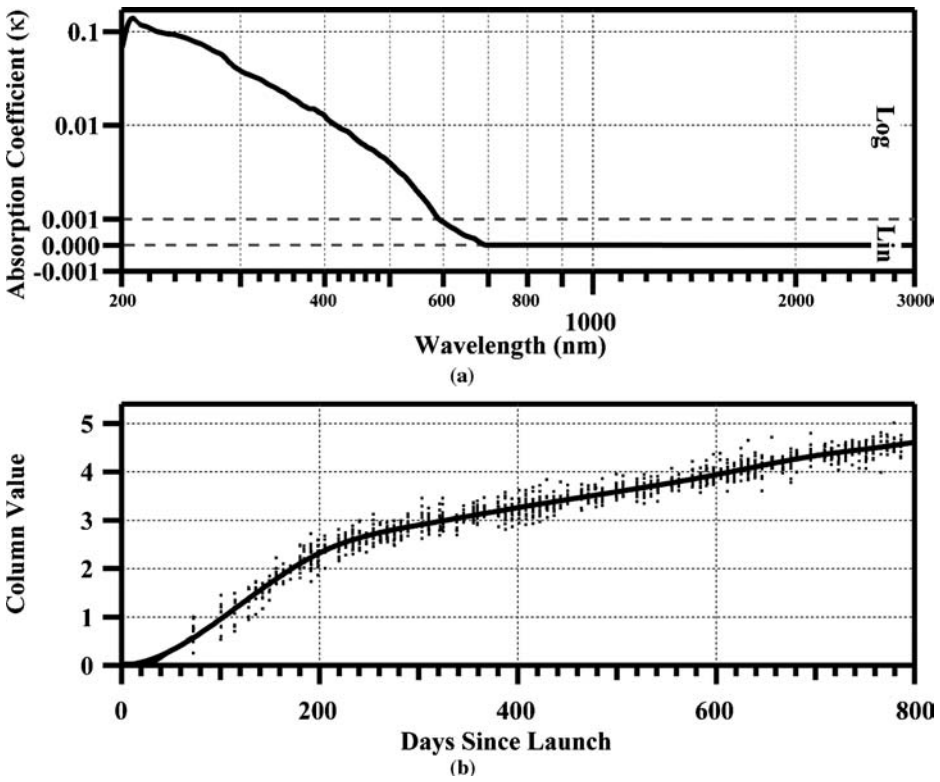

Figure 7. Panel (a) shows the time-independent absorption coefficient derived from ratios of ESR full scans and UV diode data below 300 nm. This figure is plotted as a log scale for κ value greater than 0.001, and as a linear scale below that value to indicate the function's decent to a zero value. Panel (b) shows the growth of the column layer over the course of the mission. The data is derived from prism transmission calibration experiments; the line in this panel shows the b-spline model fit to the individual data points at different wavelengths (shown as symbols). The value of prism degradation at any given time is found by applying these data to Equation (6).

The in-flight transmission measurement (mode 1 of Table I) corresponds to Equation (6), but with a different initial transmission: $\mathcal{T}'_0 = \mathcal{T}'_{0\,\text{prism}} \times \mathcal{T}'_{0\,\text{calibrator}}$. The first step in the process is to iteratively find the best values of $\mathcal{T}'_0(\lambda)$ and $C(t)$ that simultaneously minimizes the differences for all wavelengths used in mode 1 of Table I:

$$C(t) = \frac{-1}{\kappa(\lambda)} \ln\left(\frac{(\mathcal{T}'(t,\lambda))}{\mathcal{T}'_0(\lambda)}\right). \tag{8}$$

Values for $C(t)$ are then found for all value of t and λ. The $C(t)$ used for the data processing is obtained from a b-spline fitting to all of these values versus time (Lawson and Hanson, 1974); it is this b-spline fit that appears in Figure 7b.

As an example of the amount of observed degradation, at 393.4 nm (near the Ca II lines) the κ coefficient is 0.0136, and on mission day 600.0 (15 September, 2004) the column value is 3.941. The transmission relative to the unexposed value can be found by applying these parameters to Equations (6) and (7): $\mathcal{T}/\mathcal{T}_0 = \exp(-0.0136 \times 3.941) = 0.948$. Equivalently, the transmission of the prism has decreased by about 5.2% over the course of 600 days at this wavelength.

3.4. Φ_P: DIFFRACTION CORRECTION

The diffraction correction is defined as the fraction of light that lies within the clear aperture of the prism when it is diffracted by the entrance slit. Lawrence *et al.* (1998) discussed this diffraction transmission factor, and they demonstrated that the width and length of the slit can be treated as separable problems and the fractional loss in each axis is proportional to wavelength:

$$\Phi(\lambda) = \left(1 - a_W \frac{\lambda}{W}\right)\left(1 - a_L \frac{\lambda}{L}\right). \tag{9}$$

In this equation, W and L are the width and length of the entrance slit after applying the slit temperature correction discussed in Section 3.2. The dimensionless coefficient, a, is obtained from the convolution of the 0.5° projected solar disk and the rectangular slit:

$$a_W = \frac{-\Delta W}{\lambda} = \frac{1}{\pi^2 \theta_P}\left\{\frac{2 - 2\sqrt{1-\varepsilon^2}}{\varepsilon^2}\right\}. \tag{10}$$

In this equation, θ_P is the half angle subtended by the prism and ε is the ratio of the solar angular radius to the prism half angle. An analogous equation can be written for the slit height. For the SIM geometry, these factors are tabulated in Table II.

TABLE II

Slit diffraction parameters, a_W, a_L.

	Slit width	Slit length
Prism half angle (°), θ_p	0.03124	0.02250
Solar radius (°)	0.00436	0.00436
ε	0.139661	0.193944
a, $\Delta W/\lambda$	3.2593	4.5471
Example wavelengths (nm)	$\Phi(\lambda)$	
250	0.99715	
500	0.99431	
1000	0.98862	
2500	0.97158	

4. SIM Detector Characteristics and Calibrations

4.1. ESR OPERATION AND CALIBRATION

The electrical, mechanical, thermal, and optical properties of the ESR detector are discussed in Section 2.3.1 of Harder *et al.* (2005). This section describes the characterization of the detector and the terms that relate to the phase sensitive detection at the shutter fundamental. Additionally, the ESR absorption factor, α_λ, introduced in Section 3 is presented here.

In the following analysis, a tilde ($\sim$) represents complex numbers and an arrow ($\rightarrow$) denotes a times series of numbers, corresponding to each data point. The detector measurement equation can then be represented by the equation

$$\tilde{P}_{\mathrm{ESR}} = \frac{1}{M}\frac{V_7^2 R_{\mathrm{H}}}{(R_{\mathrm{S}}+R_{\mathrm{H}})^2}\left\{\frac{1+\tilde{G}}{\tilde{G}}\frac{\tilde{Z}_{\mathrm{H}}}{\tilde{Z}_{\mathrm{R}}}\right\}\frac{\vec{\tilde{p}}\cdot\vec{D}}{\vec{\tilde{p}}\cdot\vec{Q}}, \tag{11}$$

where $\tilde{P}_{\mathrm{ESR}}$: detected power; M: scaling factor for the data output: 64 000 is the data number for 100% duty cycle of the pulse width modulator; V_7: value of the 7.1 V reference; $\frac{R_{\mathrm{H}}}{(R_{\mathrm{S}}+R_{\mathrm{H}})^2}$: voltage divider ratio of the series heater resistors; $\frac{1+\tilde{G}}{\tilde{G}}$: closed-loop gain from an open-loop servo gain of $\tilde{G}$; $\frac{\tilde{Z}_{\mathrm{H}}}{\tilde{Z}_{\mathrm{R}}}$: equivalence ratio; $\frac{\vec{\tilde{p}}\cdot\vec{D}}{\vec{\tilde{p}}\cdot\vec{Q}}$: projection of the data onto shutter waveform (see Section 4.1.2); $\vec{D} \equiv D_j$: time series of data numbers from the DSP; $\vec{Q}$: shutter transmission square wave, 0 or 1; $\vec{\tilde{p}} \equiv \exp(i\,2\pi f_1 t_J) f_1$: shutter fundamental frequency; t_J: time of each data point.

The DSP data numbers $\vec{D}$ (Harder *et al.*, 2005), are produced at a rate of 100 s^{-1} and can be decimated by factors of 1, 2, 5, 10, or 20 for telemetry. Typically, the data stream is decimated by a factor 10. The ESR data numbers are a linear function of the detected power, and conceptually the ESR power (P_{ESR}) can be written:

$$P_{\mathrm{ESR}} = A_{\mathrm{P}} \times D, \quad \text{where} \quad A_{\mathrm{P}} = V_7^2 \frac{R_{\mathrm{H}}}{(R_{\mathrm{H}}+R_{\mathrm{S}})^2}\frac{1}{M}. \tag{12}$$

A light chopper then modulates P_{ESR} (Equation (12)) and converts it into the AC waveform $\tilde{P}_{\mathrm{ESR}}$.

The ratio of thermal impedances to the ESR thermistor, for radiation input and heat input, $\tilde{Z}_{\mathrm{R}}/\tilde{Z}_{\mathrm{H}}$, gives the equivalence between replacement heater power and radiant power. This equivalence ratio is determined from a model of the heat flow on the SIM bolometer as a function of frequency. The details of this model are beyond the scope of this paper, but because of the high thermal conductivity of diamond, the in-phase component of equivalence is within 10 ppm of unity. The out-of-phase component is near 3000 ppm due to mismatched delays, but this is not relevant to the determination of absorbed power.

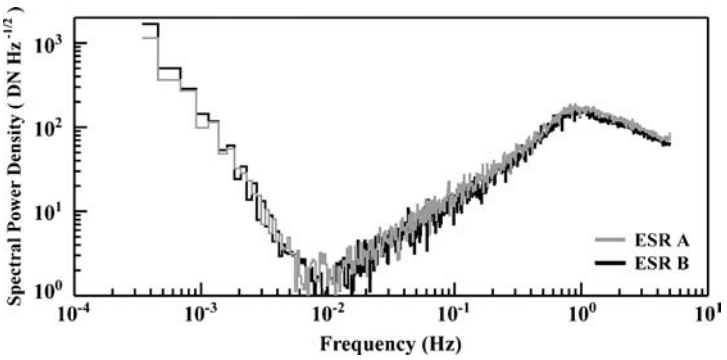

Figure 8. The noise spectral power density as a function of frequency of the two SIM ESR detectors while in flight. The minimum in the noise corresponds to the point where 1/*f*-type noise approximately equals the excess noise on the bolometer thermistors.

4.1.1. *Detector Performance and Servo Gain Recalibration*

The SIM ESR is auto-balanced by a servo-loop and the components of the loop were described in Harder *et al.* (2005). The performance of the ESR can be determined by analysis of the detector's noise spectrum. The spectrum is obtained by operating the detector in the dark for long time periods compared to shutter period, and using Fourier analysis to characterize the noise spectrum. Figure 8 shows the noise spectral power density in terms of data numbers (DN) as a function of frequency and was measured with the instrument on-orbit. The detectors show a very characteristic pattern with 1/*f* noise dominating at the lowest frequencies and with a rising excess thermistor noise power to a frequency of about 1 Hz where the servo-loop gain drops to a value near 1.0. The minimum in the noise power density at 0.01 Hz corresponds to the location where the contributions of these two noise sources cross and become comparable in magnitude. This cross over point determines the optimal shutter frequency to operate the instrument. At 0.01 Hz, the noise power is $\sim$2 DN/$\sqrt{\text{Hz}}$ and with a 200 s integration period, the noise on the measurement is $\sim$ 0.3 nW; this is the condition used for the ESR table measurements. For the ESR full scans, the instrument is operated with a 0.05 Hz shutter frequency, where the noise is a factor of 5 higher, for a 40 s dwell time per prism step giving a noise floor of $\sim$2 nW. The conditions used for this scan represent a compromise between low noise and the length of time required to complete the measurement.

The closed-loop gain is a first-order term in the ESR measurement equation (Equation (11)) and its value must be monitored throughout the flight to assure that changes in electronic component values do not change (degrade) over the course of the mission. The open-loop gain of the system can be determined in-flight by injecting a digital square wave at the shutter frequency into the servo-loop before the pulse width DAC and then measuring the system's response to this perturbation; this square wave is referred to as a feed-forward signal. The action of this feed-forward signal can be written as a control loop equation where G is the unperturbed

gain, FF is the magnitude feed-forward signal, and 'out' is the output of the control loop. This equation can then be solved for the open-loop gain of the system:

$$\text{out} = \text{FF} - G \times \text{out} \Rightarrow G = \frac{\text{FF}}{\text{out}} - 1. \tag{13}$$

Figure 9 is an example of data acquisition and the gain calculation for an in-flight calibration in February of 2005. Figure 9a shows data for a 20 s feed-forward period: a 40 min time series of ESR data is collected in the feed-forward mode and about 100 cycles are co-added to reduce random noise, and the mean value is subtracted. The detector response (the variable 'out' in Equation (13)) is shown as a gray trace, and the driving feed-forward waveform (FF) is the dotted black trace. The feed-forward waveform consists of adding in a digital value of 8000 during the first half of the period, and subtracting 8000 during the second half. In this way, the system must respond to an instantaneous change of 16 000 DN at $t = 0$ and $t = 10$ s and then settle to its balanced value. If the system was perfect, the

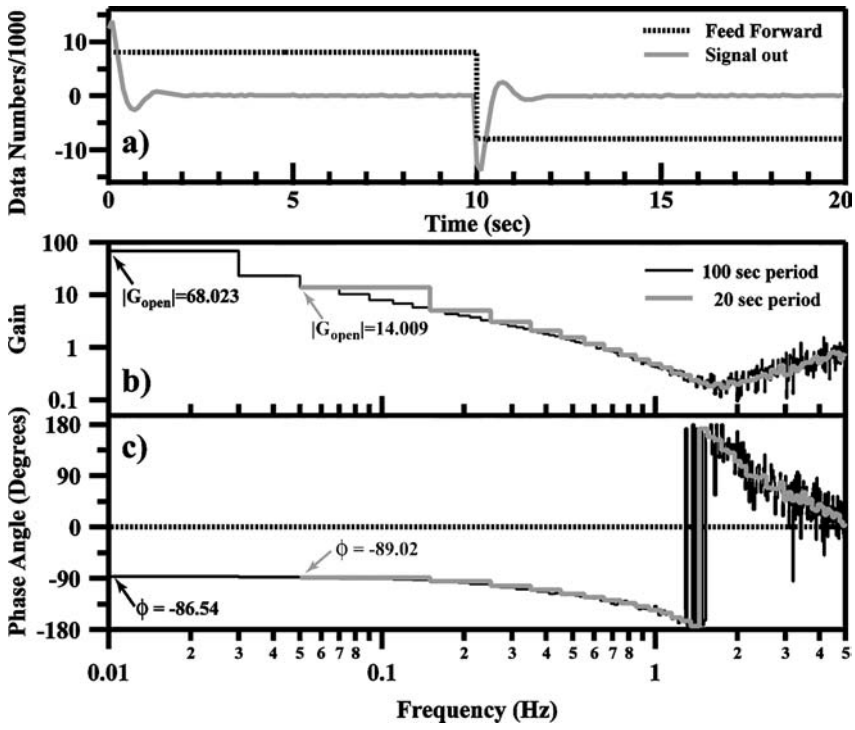

Figure 9. Gain measurements for the ESR. Panel (a) shows a time series of the SIM ESR (*gray trace*) and the feed-forward pulse (*dotted black trace*) that is driving the detector's response; the graph is for a 20 s period on the feed-forward pulse. Panels (b) and (c) show the measured gain and phase when the time series data of panel (a) is processed by Equation (13). These graphs show the results for both 100 (*black*) and 20 (*gray*) second feed-forward periods. The open-loop gain and phase at the shutter fundamental are marked on the graphs.

peak values at $t = 0$ and 10 s would be $\pm 16\,000$. The gain is found by separately performing the Fourier transforms of 'FF' and 'out' and applying Equation (13) at each frequency. The open-loop gain, G_{open}, is the modulus of G, and the phase (ϕ) is the argument and the frequency dependence of these terms are shown in Figure 9b and c, respectively. The open-loop gain attains its maximum value at the fundamental, and decreases to its minimum value at about 1.5 Hz where the phase lags by 180°. Because the incoming light from the SIM spectrometer is chopped by a shutter, only G_{open} and ϕ at the fundamental frequency are needed to calculate the closed-loop gain for the measurement equation seen in Equation (12). These values are noted in the figure for both the 100 and 20 s shutter periods. The gain and the phase have been tracked throughout the first 2 years of the SORCE mission, and they are constant and without a discernable trend to 0.1% throughout this period.

4.1.2. *Projection Operator for Phase Sensitive Detection*

The projection operator, $\vec{\tilde{p}}$, presented in Equation (11) is a discrete Fourier filter that operates on M shutter cycles and N data points per cycle; the M-cycle filter contains MN points. The most typical values for SIM measurements are $M = 2$, and $N = 1000$ for the 100 s shutter period used for ESR table measurements or $N = 400$ for the ESR full scan. The projector has the following properties:

a. It defines a smooth window function, W_J, where the data index J runs 0 to $MN - 1$. W_J goes to zero at the edges of the data block, and is optimized to reject background drift, shutter harmonics, and noise.
b. Multiply W_J by $e^{-i2\pi ft}$ where f is the shutter frequency and t the time of the data point.

The complete projector function can then be written:

$$\tilde{p}_J = W_J \tilde{\Theta}_J \equiv \vec{\tilde{p}}. \tag{14}$$

The window function is constructed by convolving M identical boxcar windows, then centering the result on the data window. These boxcars are all exactly N points wide and give zeros in the frequency response at the shutter cycle harmonics. The cosine and sine waveforms are expressed as complex exponential function:

$$\tilde{\Theta}_J = \exp\left[-i\frac{2\pi J}{N} + i\phi\right] \equiv \cos\left[\frac{2\pi J}{N} - \phi\right] - i\ \sin\left[\frac{2\pi J}{N} - \phi\right]. \tag{15}$$

The phase angle ϕ is arbitrary if the same phase angle is used in the projection of the shutter waveform. Since ϕ is arbitrary, it is set to zero for simplicity. Figure 10 shows W_J, the shutter waveform, and the real and imaginary parts of $\vec{\tilde{p}}$ for the case of $M = 2$ as calculated by Equations (14) and (15).

The last step is to perform the dot product by multiplying the Jth data point and the projector element and summing all elements in the data block. This same

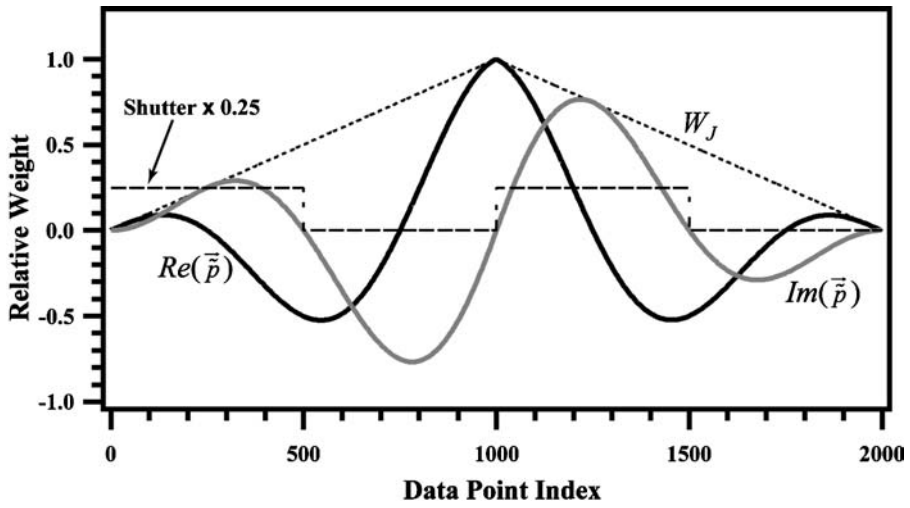

Figure 10. Waveforms of W_J, the shutter, and the real and imaginary parts of $\vec{\tilde{p}}$ for the case of $M = 2$.

process is applied to the idealized shutter wave form, Q_J, and these two quantites are ratioed to ensure proper scaling of the data numbers:

$$\frac{\vec{\tilde{p}} \cdot \vec{D}}{\vec{\tilde{p}} \cdot \vec{Q}} \equiv \frac{\sum_{J=0}^{MN-1} \tilde{p}_J D_{NK+J}}{\sum_{J=0}^{MN-1} \tilde{p}_J Q_{NK+J}}. \tag{16}$$

4.1.3. *Absorptance of Nickel Phosphorus Black*

The absorptance of the bolometer, α, results from the combined effects of the absorptance of the nickel phosphorous (NiP) and the return reflectance of the aluminized hemisphere of the ESR cavity (see Harder *et al.*, 2005, Section 2.3.1, for more discussion on the optical properties of the ESR). The value of α is wavelength-dependent and is found by summing the light absorption through the multiple absorption/reflection light path between the bolometer and its surrounding reflective hemisphere.

Assume that the intensity of light entering the ESR detector is I_o and the NiP surface of the bolometer has an absorptance ρ. On first contact with the bolometer the fraction of light absorbed is ρ. The intensity of light diffusely scattered off of the bolometer, β, is then $I_o\beta$ where $\beta = (1 - \rho)$. This light is then reflected off of the aluminum hemisphere with reflectivity, r, and re-directed to the bolometer with an intensity of βr. This light will again be absorbed, and the process is repeated until the intensity becomes diminishingly small. The overall efficiency of this process can be written as an infinite series and summed because it is a geometric progression:

$$\alpha I_0 = I_0\rho + I_0\beta r\rho + \beta^2 r^2\rho + \cdots + I_0\beta^n r^n\rho + \cdots \quad \text{with } 0 < \beta, \quad r \leq 1,$$

$$\alpha = \rho(1 + \beta r + (\beta r)^2 + (\beta r)^3 + \cdots + (\beta r)^n + \cdots) = \rho\left(\frac{1}{1 - \beta r}\right). \tag{17}$$

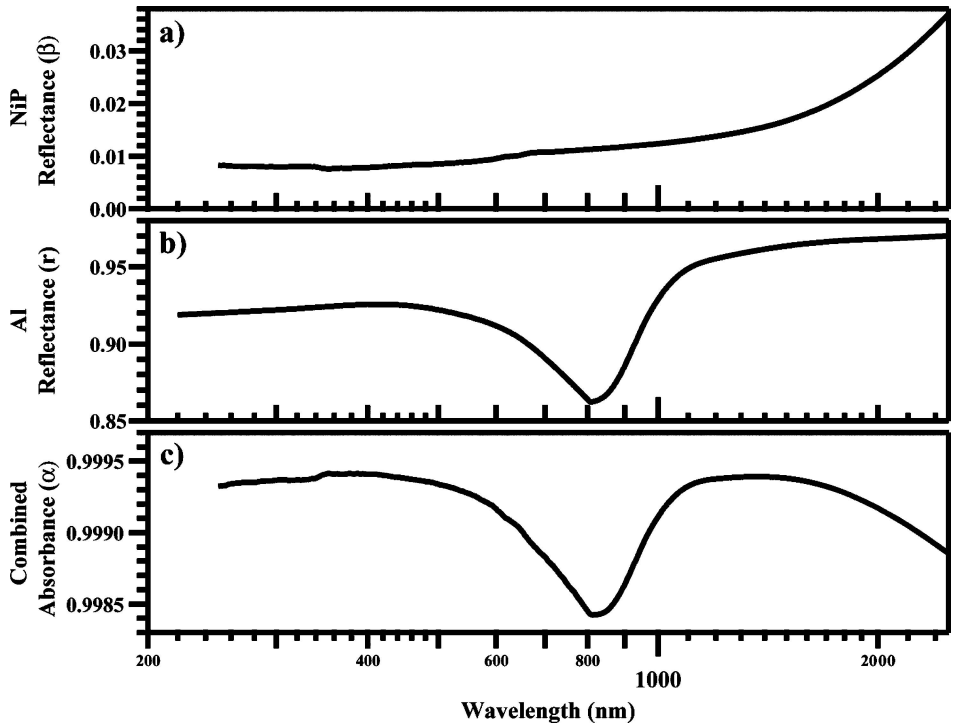

Figure 11. The reflectance of the NiP surface (β) of the bolometer; here $\beta = (1 - \rho)$, where ρ is the absorptance (panel (a)). Panel (b) is the reflectance of the hemispherical reflector surrounding the bolometer (r). Panel (c) is the combined absorbance (α) of the sphere and the bolometer as calculated from Equation (17) assuming no optical aberrations.

Figure 11 shows the wavelength dependence of ρ, r, and α. This figure shows that the hemispherical reflector significantly increases the blackness of the bolometer. In this figure, and in the derivation of Equation (17), it is assumed that the optical efficiency of the cavity is 1, and in other words, every ray reflected off of the bolometer is re-collected because of the hemispherical cavity. This assumption most likely is not true because of aberrations, particularly at longer wavelengths. Laboratory tests are needed to test this assumption. The nickel phosphorous black used for the SIM ESR bolometers was developed and produced by Custom Microwave Inc. (Longmont, CO) in conjunction with our laboratory, and a test article produced by the same production method used for the SIM bolometers was subsequently tested by Ball Aerospace Inc. (Boulder, CO). Ball Aerospace produced a report (Fleming, 1999) on these tests. This report presents measurements of the bi-directional reflection distribution function (BRDF) and total hemispherical reflectance (THR) of this material. It is assumed that optical properties of the material tested in Fleming's report are representative of the material used for the flight bolometers. This is a reasonable assumption since the electron micrographs of the test article and the

black surface are comparable in structure. It is necessary to make this assumption since it was not possible to measure the flight component because the reflectance measurement requires a large target area so the light signal reflected off of the black samples is large enough to make a quality measurement. The quoted error for wavelengths greater than 800 nm is 0.5%, and about an order of magnitude less than this for the 250–800 nm range. This study demonstrated that the light reflected from the surface of the black is predominately diffuse with a small (<0.6%) specular reflectance component.

4.2. PHOTODIODE CALIBRATION AND DEGRADATION CORRECTION

The radiant responsivities, $\mathcal{R}_\lambda$, (units of A W^{-1}) for each photodiode are measured on-orbit by dividing the photocurrent by the power measured by the ESR using phase sensitive detection. There are a number of small, but important, complications to this process: $\mathcal{R}_\lambda$ is not constant over a typical SIM resolution element, particularly near the red cut-off of the photodiode's response curve, whereas the ESR response is essentially flat. Therefore, the convolution over the instrument function is different for these two detectors and must be accounted for in forming the ratio. Portions of the spectrum where the photodiode's response changes rapidly cannot be accurately measured by this method. Nonetheless, the highly stable geometry, wavelength knowledge, and intensity provided by the Sun makes this measurement much more accurate and reliable than an equivalent laboratory calibration. Figure 12 shows the radiant responsivity retrieved by this method for the four photodiodes used for SIM A.

The radiant responsivity curves shown in Figure 12 define the ranges over which each detector gives reliable data. The photodiodes provide complete coverage everywhere except for a small part of the spectrum between 308 and 310 (covered by the ESR). The Vis2 and IR photodiodes overlap in the 900–1000 nm region, and the best data quality in this spectral region is from Vis2 because $\mathcal{R}_\lambda$ function is

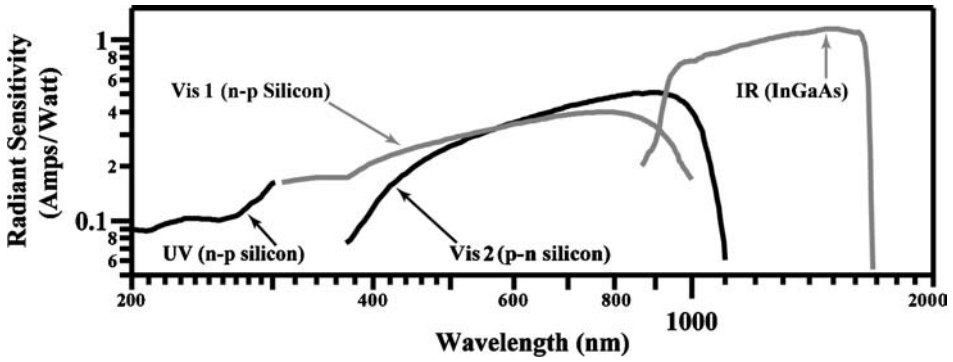

Figure 12. Radiant sensitivities for the four photodiodes used for SIM. The values are measured in-flight using the ESR to calibrate the photodiodes.

smoother. However, both silicon photodiodes have greater temperature sensitivity red-ward of the $\mathcal{R}_\lambda$ peak, so data in this regime are corrected and their usage limited because of the increased uncertainty. In summary, the operating ranges for the photodiodes that give the most reliable results are as follows: UV = 200–308 nm, Vis1 = 310–800 nm, Vis2 = 800–1000 nm, IR = 1000–1655 nm.

The photocurrent from each photodiode is measured with a radiation hardened transimpedance amplifier with an 11 Hz bandwidth, multiplexed and then converted to digital numbers with a 16-bit, bipolar, dual-slope analog-to-digital (ADC) converter. Each channel of photodiode data is sampled at 100 Hz, and then decimated at the same rate as the ESR data by the instrument's DSP. The feedback resistor for each amplifier was selected to cover most of the 2^{15} bit unipolar dynamic range of the ADC needed for each photodiode's spectral range. The converter has about 2 bits of noise per sample, so the photodiode measurements are ADC limited rather than photon noise limited. Because of this, the ultimate signal-to-noise ratio (SNR) is proportional to signal strength for a fixed integration time, and doubling the dwell time at a fixed wavelength does not improve the SNR by $\sqrt{2}$.

Since the photodiode spectral scans are used to track the orbit-to-orbit variability of the Sun (see Sections 3.2 to 3.4 of Rottman *et al.*, 2005 for more detail), their measurement precision plays an important role in interpreting solar variability. Figure 13 shows the measured photocurrent for the Vis1 photodiode as a function of CCD position and wavelength. On the right hand axis is the SNR ratio on this measurement.

The custom made photodiodes used for SIM are 10 mm × 2 mm for the three silicon photodiodes (International Radiation Devices Inc., Torrence, CA) and 8 mm × 2 mm for the InGaAs photodiode (Hamamatsu Corporation, Bridgewater,

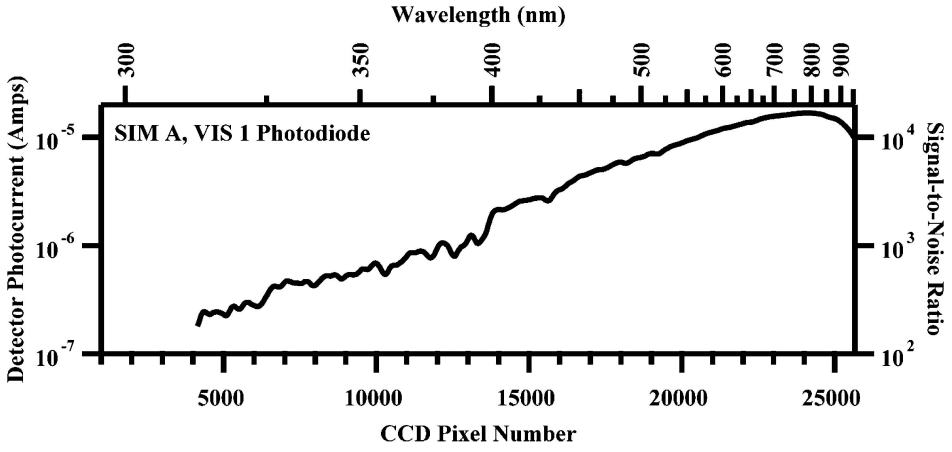

Figure 13. Raw spectral data for SIM A Vis1 photodiode. The *bottom axis* shows the CCD pixel value for the scan, and the *top axis* is the wavelength corresponding to the bottom axis. The measured detector photocurrent is shown on the *left axis*, and the approximate SNR that corresponds to the photocurrent is shown on the *right*.

NJ). The Vis1 and UV silicon photodiodes have n-on-p construction with a nitride passivated SiO_2 layer to stabilize their radiant sensitivities in the ultraviolet. The Vis2 photodiode is constructed similarly, but with p-on-n geometry. The silicon photodiodes appear to undergo a slow decrease in responsivity predominately for wavelengths longward of the responsivity peak (see Figure 12) that remains apparent in the data after prism degradation is removed. Loss of photodiode responsivity is the dominant source of instrument degradation for wavelengths greater than 650 nm where prism glass is stable (see Figure 7a). At this point in time, the radiation damage observed in the SIM photodiodes is consistent with the radiation testing described by Jorquera *et al.* (1994). They found negligible damage on the n-on-p photodiodes for the short wavelengths, and small (though not specified) damage for the long wavelengths. For the p-on-n detectors, they reported no change at 420 and 552 nm, but a 2 and 11% drop in the internal quantum efficiency at 670 and 875 nm, respectively, and for 5 MeV proton energy at a fluence of 6.0×10^8 protons cm^{-2}. The best method to correct the in-flight degradation is to match the slope of the photodiode time series to that of ESR measurements at selected wavelengths. This process is most readily done at the ESR table values. The degradation is expected to be smooth, so values between the wavelengths in the ESR table are interpolated. This method has the distinct advantage of correcting the diode degradation but not biasing the slope in the data that occurs as the intensity of the Sun decreases to the (yet unknown) solar cycle 23 minimum value over the next 3 years. The exact nature of photodiode degradation seen in-flight is still under study and, like prism degradation, will require further refinement as more data become available over the course of the SORCE mission; more detailed discussions about this degradation mechanism will be presented in subsequent publications about the SIM instrument.

5. Final Corrections and Status of SIM Solar Spectroscopy

At this juncture in time a number of additional corrections and analyses will be performed on the SIM instrument prior to assigning a final absolute calibration to the instrument. Corrections that have been implemented are:

1. The dispersion model of Section 2 and Appendix A requires slightly different parameters for each detector. In particular, the wavelength scales for each photodiode detector and the ESR can be brought into agreement with the solar spectrum of Thuillier *et al.* (2003) to within ± 0.02 nm by assigning independent wedge angles, θ_{P}, for each of the focal plane detectors, and by changing the effective sub-pixel size, C, on the CCD from 1.3 μm to 1.2886 $\mu\mathrm{m\,pixel}^{-1}$ (see Equations (A.1) and (A.2)). This result was obtained by convolving the 1.3 nm-resolution Thuillier *et al.* Composite 1 spectrum with the wavelength-dependent SIM instrument function in the 300 –900 nm range. The two spectra are then processed to a zero mean

differential spectrum and the θ_P and C parameters of the dispersion model are varied using Levenberg–Marquart minimization (Press *et al.*, 1992) until a minimum in the sums of squares difference between the two spectra is obtained. In using this method to find the best prism wedge angle for each detector, the worst case difference is about 0.013° out of a wedge angle of 34.497°. There is only a single prism and it is not possible to have different wedge angles, but making the correction in this parameter fixes a problem most likely caused by slightly different refraction angles produced by spherical surfaces on the prism. The dispersion equations of Appendix A do not account for curvature of the prism faces. Studies of prism refraction based on non-sequential ray tracing may lead to an improved physical understanding and correction to this problem.

2. The solar irradiance variations in the visible and near IR are on the order of 0.05–0.1%, so very small shifts in wavelength produce comparable discontinuities in the time series. The effect was clearly seen in the first 10 months of operation of SIM with the occurrence of a problem related to commanding CCD position system. This problem caused the signal on the CCD to saturate and produced a non-linear response in the drive's servo system that could not be detected in the drive housekeeping channels. Different CCD settings produced different levels of saturation and therefore a different drive response. This problem has been corrected by identifying the CCD settings that prevent CCD saturation, and the affected spectra are being corrected in ground processing with a spectral shift-stretch algorithm. The affected spectra are shifted and stretched with respect to a standard SIM spectrum without the CCD position non-linearity. The algorithm used to perform this re-mapping of the CCD position (C) converts the measured spectra into a zero-mean differential spectrum and uses a golden section search over a limited range of C values to align the spectra. This process is performed for each detector and over the full operating range of the prism drive. Prior to performing the wavelength alignment, the data are corrected for degradation so spectral slope does not bias the peak finding of the golden section search. The transfer function between the saturated and non-saturated drive positions is fitted with a third-order polynomial and then applied to the affected spectra.

The analysis of NiP absorptance, and therefore the overall efficiency of the ESR, requires further analysis and ground-based experimental verification. This study is being performed on a flight witness ESR made with the same components as the flight detectors. These measurements will impact the discussion of Section 4.1.3. Additional information on the efficiency of the detectors will be obtained through the on-orbit comparison of the two SIM spectrometers. In addition, end-to-end analysis of the prototype SIM responsivity are being planned and may provide a more definitive validation of the parameter used to derive the solar irradiances for the SIM measurements.

At the present time, and for the purpose of comparing SIM spectral irradiance time series to other measurements of solar activity, such as the Mg II core-to-wing ratio and TSI (see Rottman *et al.*, 2005), a relative calibration factor is applied to the current SIM radiometric calibration. This correction factor smoothly brings the SIM data into agreement with Thuillier *et al.* (2003) for the infrared and visible, and with UARS SOLSTICE for the 200–300 nm spectral regions. This adjustment is only significant for wavelengths longer than 600 nm and has a very smooth wavelength behavior. Thus, all spectral features present in the SIM spectra are measured and are not a consequence of these adjustments. This adjustment is complemented by a final correction through a wavelength-independent coefficient that makes the integral of SIM irradiance in the 200–1600 nm range equal to 1225 Wm^{-2}. This value assumes the TIM TSI value of 1361 Wm^{-2} and estimates the irradiance in the 1.6–10 μm wavelength range at a value of 136 Wm^{-1} using the Fontenla *et al.* (1999) spectral synthesis calculation. This final correction is only about 1% and within the absolute accuracy of our measurements at this time.

Figure 14 represents the current spectrum with a wavelength accuracy of ± 0.02 nm and an overall radiometric accuracy of about 1%. The top panel of the graph shows the irradiance spectrum, and the lower panel shows the average disk brightness temperature (Fontenla *et al.*, 1999). This plot is from 210 to 1650 nm covering the range of the SIM photodiodes. The solar spectrum in the

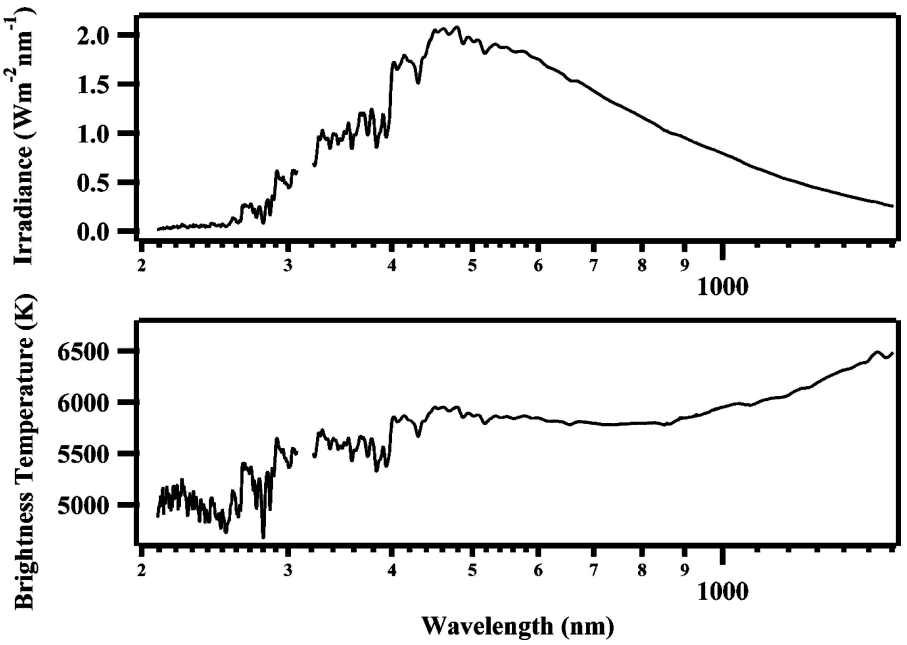

Figure 14. Current SIM solar spectrum. The *top panel* shows the spectrum in terms of irradiance, and the *lower panel* is the same data in terms of brightness temperature.

TABLE III
Current estimates of the calibration parameters for the SIM instrument.

Parameter (units)	Magnitude/range	Uncertainty
Solar distance (ppm)	+33116 to −33764	1
Doppler (ppm)	43	1
Wavelength (nm)	200–1650	$\sim 0.02 \pm (150 \times 10^{-6}) \times \lambda$ (worst case)
Instrument function area	0.58–34.5	∼0.4%
Slit parameters		
Width (μm)	300.0	0.5 ± 0.03
Area (mm^2)	2.1	$3 \times 10^{-5} \pm 2 \times 10^{-5}$
Component metrology (mm)	0 – 400 mm	0.01
Prism transmission		
Value (%)	0.55–0.77	0.1% 200–700 nm
		∼1% 1000–2700 nm
Degradation correction	∼0.to 0.65	∼0.1%
Diffraction correction (%)	0.3–2.2	∼0.01
ESR parameters		
Standard volt (V)	7.1615 V	10 μV
ESR absorptance (%)	∼99	+0 to −1 (200–700 nm)
		+0 to −10 (700–2700 nm)
Closed-loop gain	15.086	1×10^{-4} (0.05 Hz)
	73.205	3×10^{-5} (0.01 Hz)
Equivalence (ppm)	100	60

1650–2700 nm range is still under study and is not reported here due to additional analysis needed as related to incomplete pre-flight calibrations in this wavelength range and to needing improved processing algorithms for these data.

Table III provides a summary of the magnitude or range of values associated with terms in the measurement equation scheme presented in Figure 2, and the current accuracy estimates of the calibration parameters discussed in this paper. Refinements in the error estimate will occur with additional analyses and studies of ground witness components. In particular, additional work must be done on the optical efficiency of the ESR, which currently is the largest source of uncertainty in the measurement. The entry in Table III for the important solar distance and Doppler corrections are derived from the JPL Ephemeredes (Standish, 1982), and are included in standard SORCE data processing. The wavelength uncertainty of $0.02\,\text{nm} \pm (150 \times 10^6) \times \lambda$ is derived from the accuracy adjustment of the wavelength scale to the spectrum of Thuillier *et al.* (2003) and the worst case precision based on the variable resolution of the instrument. A more refined precision can be found from the ±1 subpixel CCD reproducibility of the prism drive and an analysis of Equation (A.4).

Acknowledgements

The authors would like to acknowledge the contribution of the entire LASP Engineering and Calibration Groups for their patient and thorough efforts on the calibration of this instrument. In particular, we would like to thank David Crotser, Mathew Triplett, Karl Heuerman, Anthony Canas, Miriam Adda, and Byron Smiley whose work forms the basis of this paper. This research was supported by NASA contract NAS5-97045.

Appendix A

This Appendix is associated with Section 2, and describes the equations that relate the measured prism rotation angle to refraction angle and wavelength. The terms and angles are defined in Figure 3.

A.1. Prism incident angle measurement: γ from CCD subpixel position

The prism incident angle, γ, is found from the imaging behavior of an off-axis spherical mirror (see Section 2.3.3 of Harder *et al.*, 2005 for a description of the CCD encoder system):

$$\gamma = \gamma_z + \frac{1}{2}\tan^{-1}\left(\frac{C - C_z}{F_{\mathrm{REF}}}\right). \tag{A.1}$$

In this equation the subscript z is the CCD subpixel count and corresponds to the condition that the centroid of the image on the CCD is aligned with the center of the spectrometer entrance slit in the dispersion plane. F_{REF} is the focal length of the spherical mirror used with the focal plane CCD. For the SIM instrument, C corresponds to 1/5th of a CCD pixel width or 1.3 μm.

A.2. Refraction angle calculation: ϕ from γ and n

Equation (2) in Section 2 can be solved for the angle ϕ and knowing the focal length of the prism (F), the spectral coordinate y can be obtained:

$$\phi = \gamma - \sin^{-1}\left(n \sin\left\{2\theta_{\mathrm{P}} - \sin^{-1}\left(\frac{\sin(\gamma)}{n}\right)\right\}\right) \text{ and } y = F\tan(\phi). \tag{A.2}$$

The index of refraction of fused silica is calculated from the three-term Sellmeier equation that is valid to about 10 ppm at 20 °C (Malitson, 1965). See also discussion

of Equation (2) in Harder *et al.* (2005):

$$n_{20}(\lambda) = \sqrt{1 + \sum_{j=1}^{3} \frac{\lambda^2 K_j}{\lambda^2 - L_j}}. \tag{A.3}$$

Malitson also provides the temperature dependence dn/dT used to correct for wavelength shifts that occur as the prism temperature changes during in-flight operation.

The wavelength of an observation occurs when $y(n, \phi) = y_{\mathrm{d}}$, where y_d is the focal plane location of one of the five focal plane detectors. Thus, at a given prism incident angle, five different wavelengths are detected. Likewise, a specified wavelength can be delivered to a specific detector by changing ϕ. This topic is discussed in Section 2.3.2 of Harder *et al.* (2005) in the context of the instrument's functional capabilities.

A.3. Index of refraction calculation: n from γ and ϕ

Solving Equation (A.2) for n gives the index of refraction strictly from prism geometry for rotation angle:

$$n = \frac{1}{\sin(2\theta_{\mathrm{P}})} \sqrt{\sin^2(\gamma) + 2\cos(2\theta_{\mathrm{P}})\sin(\gamma)\sin(\gamma - \phi) + \sin^2(\gamma - \phi)}. \tag{A.4}$$

Numerically inverting Equation (A.3) and accounting for dn/dT determines the wavelength. Newton's method (Press *et al.*, 1992) provides an efficient numerical solution for this inversion.

A.4. Prism incident angle calculation: γ from n and ϕ

Solving Equation (A.2) for γ gives the prism rotation angle:

$$\sin(\gamma) = \sqrt{\frac{\cos(\phi)\sin^2(2\theta_{\mathrm{P}}) + X\cos(2\theta_{\mathrm{P}})\sin^2(\phi) + \sin(\phi)\sin(2\theta_{\mathrm{P}})\sqrt{(\cos(2\theta_{\mathrm{P}}) + X\cos(\phi))^2 - (1 - X)^2}}{2X(\cos(2\theta_{\mathrm{P}}) + \cos(\phi))}}$$

with

$$X \equiv \frac{1}{n^2}. \tag{A.5}$$

Equation (A.1) is then solved for C and insertion of γ from Equation (A.5) gives the value of C as a function of ϕ and n.

Appendix B

Appendix B is associated with Section 3.2, and describes the experimental methods for slit width calibration (Section B.1) and slit area calibration (Section B.2).

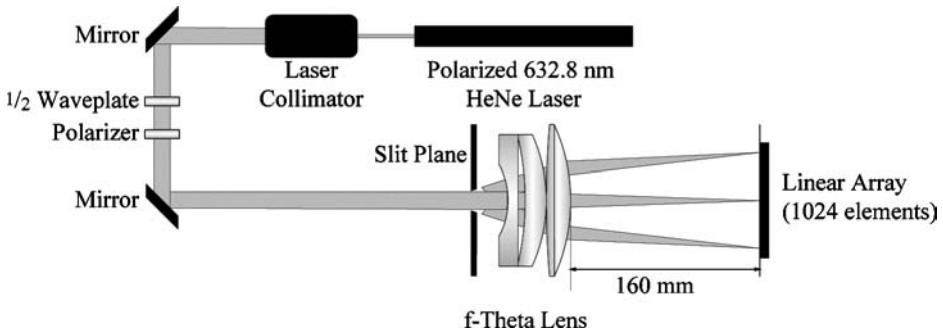

Figure B.1. Apparatus used to measure slit diffraction. An amplitude-stabilized laser beam is expanded and polarized and then impinges on the slit plane. An *f*-theta lens then images the diffraction pattern onto a linear array. Slit widths are determined from a least-squares fit of the diffraction pattern.

B.1. SLIT WIDTH INFERRED FROM THE DIFFRACTION PATTERN OF A 632.8 NM LASER

The most convenient method for creating a far-field diffraction pattern at a finite distance is to employ a lens in the Fourier-transform configuration with the slit and detector placed at the conjugate focal points of the lens. It is important that the lens has low distortion and that its position in the detector focal plane linearly relates to the diffraction angle. Figure B.1 shows the apparatus used to make this slit diffraction measurement. An amplitude stabilized laser beam is collimated with a zoom expander and the quality of collimation is examined with a shear plate. The beam polarization is established with a polarizer so the polarization direction is parallel to the long-dimension of the slit. A $\frac{1}{2}$ waveplate is then inserted in the beam as a variable attenuator to keep the light level within the linear operating range of the detector. The expanded laser beam then impinges on the slit plane where both flight slits and a custom calibration target are mounted. The diffracted radiation is then passed through an *f*-theta lens (Optische Werke G. Rodenstock, München, Germany). This lens conserves the angle (θ) in focal plane instead of $\tan(\theta)$, which is important since the observed diffraction depends on θ as well. The lens is optimized to work at 632.8 nm and the air wavelength is corrected to atmospheric conditions using Edlen's (1953) formulation. The lens has a distortion less than 0.1% for off-axis rays within a 25° light cone; for this experiment, only about 6° of this light cone is used for the measurement. The diffracted light is then imaged onto a 1024 element linear array with 20 μm wide $\times$ 2.5 mm tall pixels on a 25 μm pitch (Hamamatsu S3903-1024Q). The photoresponsivity non-uniformity (PRNU) is measured and removed from the data prior to analysis.

The calibration mask (Photo Sciences Inc., Torrance, CA) consists of a series of nine double slits and nine single slits etched onto a chrome-on-fused silica plate. The double slits have a 4 μm width and spacing of 200, 300, and 400 μm and are used to calibrate the apparatus. The single slits have widths of 100, 300, and 400 μm

and are used to check the calibration. When measured with the apparatus shown in Figure B.1, the calibration mask is placed in the light beam perpendicular to its direction of propagation; the light beam encounters the glass substrate before the chrome layer containing the slits, and in this way its refractive properties do not disturb the measurement. After manufacturing the plate, Photo Sciences measured the widths and spacing between the slits with a Nikon 2i metrological microscope and quoted an uncertainty of $\pm 0.5\ \mu$m for measurements in the 0.1–150 mm range; their microscope calibration is traceable to NIST standards. The quoted uncertainty on this measurement is larger than the requirement for the flight slits, but the calibration mask is a ground witness, and future improvements in dimensional measurements of the mask will directly translate into a refined measurement of the flight slits. The agreement between Photo Sciences' microscope measurement and the result of this experiment are at least as good as the quoted $\pm 0.5\ \mu$m uncertainty.

The diffraction pattern from two slits separated by a distance a, with a width, W, produce an apodized cosine wave pattern that is described by the Fraunhofer theory of slit diffraction (Jenkins and White, 1976):

$$I(\theta) = 4I_{\mathrm{o}}\left(\frac{\sin^2\beta}{\beta^2}\right)\cos^2\alpha, \quad \text{where} \quad \beta = \frac{\pi W}{\lambda}\sin\theta, \quad \alpha = \frac{\pi a}{\lambda}\sin\theta, \quad \theta = \frac{f\,(y)}{F}. \tag{B.1}$$

In this equation, the diffraction angle, θ, is determined from a polynomial function of position, y, along the linear diode array, and the focal length of the lens. Least-squares fitting of this pattern to the calibrated slit mask is used to remove lens distortion, and precisely measure the focal length of the *f*-theta lens, thereby establishing the scale of the apparatus so single slit widths can be determined when mounted in the apparatus. Figure B.2(a) shows the measured double slit pattern, the modeled output, and the fit residuals. The modeled data are found from a Levenberg–Marquardt least-squares minimization (Press *et al.*, 1992) that fits the experimental data to Equation (B.1) with additional non-linear parameters to adjust the scale, offset, slit width (held constant here), lateral shift with respect to the center of the array, and slope across the array. The fitting is performed on the noise-weighted signal. Figure B.2(a) shows a narrow light spike on the central fringe. This is caused by collimated laser light passing through the chrome plating on the calibration mask, which is then imaged into the CCD. The mask has an optical density of 5.0 (0.001% transmission), so this problem was expected and an algorithm was developed to account for its influence (see discussion below). The measurement of the flight slits is not disturbed by this problem.

Figure B.2(b) shows a similar plot for one of the slits used for the flight instrument; the graph is on a log scale to emphasize the dynamic range associated with the single slit diffraction measurement. Since the least-squares analysis is weighted by the detector noise, only the first several fringes meaningfully contribute to the

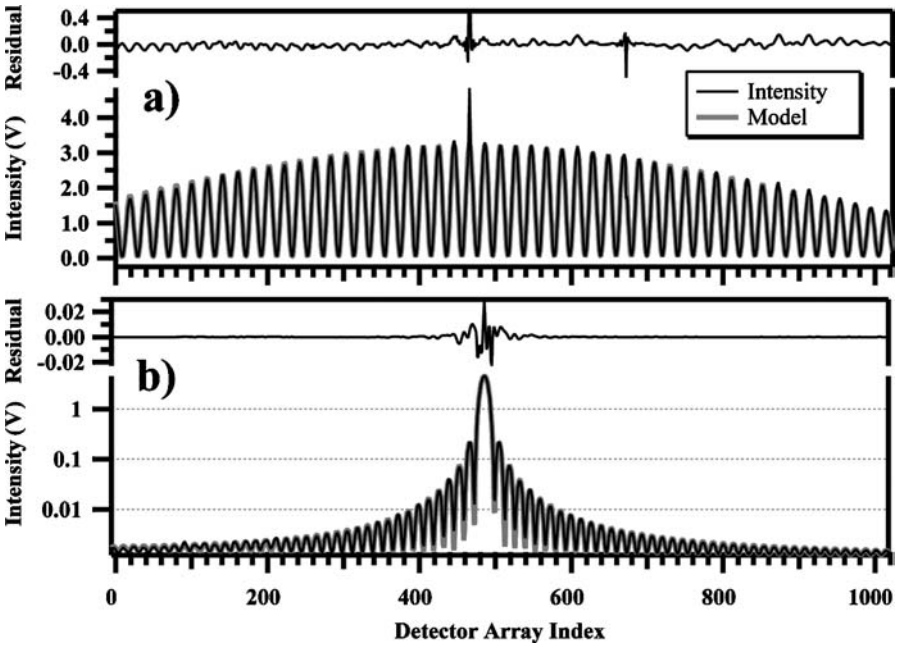

Figure B.2. Panel (a) shows the diffraction pattern generated by one of the Photo Sciences' calibrated double slits with a slit spacing of 200 μm, as well as the fitted model result and fit residuals. The central spike, caused by light transmission through the mask, is apparent in both the data plot and the residual plot. The axis range on the residual plot is set to show the fit quality in the wings of the diffraction pattern, so the central spike is off-scale. Panel (b) shows a single slit diffraction for one of the flight instrument's entrance slit. The intensity scale is logarithmic to emphasize the structure in far wings.

quality of the fit. The same least-squares method described for the double slit measurement applies to the single slit, but uses the focal length and distortion terms as fixed parameters, and fits the data using the Fraunhofer single slit diffraction law:

$$I(\theta) = 4I_{\mathrm{o}}\left(\frac{\sin^2\beta}{\beta^2}\right), \quad \text{where} \quad \beta = \frac{\pi W}{\lambda}\sin\theta, \quad \theta = \frac{f(y)}{F}. \tag{B.2}$$

Prior to performing the flight slit calibrations, the validity of the double slit experiment is verified by measuring the widths of the single slits in the calibration mask. The light leak discussed in the previous paragraph is also present in the single slit measurement, but it is less pronounced due to the less intense light level used in this experiment relative to the double slit experiment. However, its influence on the least-squares fit is still significant because of the rapidly changing signal level associated with single slit diffraction and errors in the intensity of the central fringe have the greatest influence on the results of the fit. To account for this problem, the analysis method was expanded to include a step where the intensity of the central fringe was perturbed away from its measured value, and this data was then

least-squares fitted. The retrieved value of χ^2 is noted and this procedure is repeated until a global (but physically plausible) minimum is found. This procedure is aided by noting that Fraunhofer diffraction theory indicates that the ±first-order fringes have peak values that are 0.046 as intense as that of the central fringe. Since the first-order fringes are well outside the region affected by the light leak, a first guess of the central fringe's true intensity is set to this value.

The light leak does not greatly affect the outcome of the double slit fitting because all of the cosine lobes have approximately the same intensity over the full detected range, and so they have about the same weighting in the least-squares fit. When the analysis described in the previous paragraph is applied to the double slit problem (with modifications to the magnitude of the first guess), the analysis indicates that the light leak makes a difference in the recovered focal length of only 12.5 ppm and a difference in the distortion term of 0.25%, but the RMS value of the residual dropped by about a factor of 2. These modified values were then used as fixed parameters in the analysis of the calibration mask's single slits and the SIM slits for the flight unit. For the measured single slits on the calibration mask, this method retrieves the same slit width to better than the stated ±5 μm uncertainty. This same procedure was applied to the measurement of the slits that do not have the light leak problem; the linearity of the detector electronics is about 0.1% of full scale and this procedure introduced corrections on the order of 0.05% thereby giving reproducibility in the slit width retrievals of better than 100 ppm.

B.2. Slit area inferred from the light flux comparison with a standard aperture

The flux comparator system designed to compare SIM slit with a standard 0.5 cm^2 NIST calibrated circular aperture is shown in Figure B.3. The area ratio between the

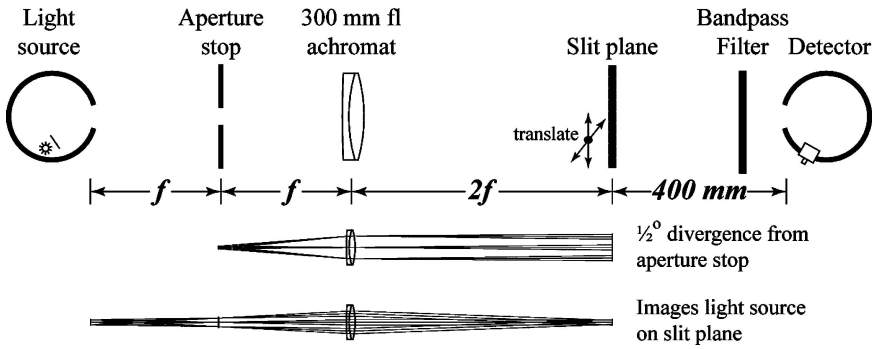

Figure B.3. The apparatus used to compare the areas of the 0.3 mm × 7 mm SIM slits to a standard 0.5 cm^2 circular aperture. The figure shows the optical arrangement based around a 300 mm focal length achromat and its associated ray traces. The slit plane is an *x*–*y* translation stage so the uniformity of the light source can be mapped in the slit plane, and the comparative measurement can be automated.

SIM slits and this standard aperture is a factor of 23.8, so the difference in intensities for uniform light will be nearly the same. This dynamic range is well within the linear operating range of photodiodes and this makes the flux comparison the most effective method to measure the area of the slits. This apparatus is similar to the one discussed by Fowler, Saunders, and Parr (2000), but has a number of attributes that make it appropriate for spectrometer slit measurements. The apparatus is based on a telecentric optical system with a 300 mm focal length achromat ($f = 300$ mm in Figure B.3) as the objective. The system's aperture stop is at a distance of f and the source and image planes are at a distance of $2f$. In this configuration, the uniform source area is imaged onto the exit plane, and the aperture stop diameter, d, is sized to produce a light beam with a 0.5° of divergence ($d = f\tan(0.5^\circ) = 2.6$ mm). This optical arrangement ensures the calibration is performed with nearly the same geometry as the Sun, and the 1:1 imaging in the slit plane gives the optimal light intensity and radiometric accuracy. The light source illuminates a 20 cm diameter integrating sphere with a 1.27 cm circular exit port; this configuration produces a spatially uniform light beam, and the lamp power was current regulated to 0.1% to reduce intensity fluctuations. After passage through the slit plane, the light encounters a 500 ± 50 nm optical filter before being detected by a 50 mm^2 silicon photodiode located inside an integrating sphere identical to the source, and the detector's photocurrent is readout with a precision ammeter. The detector sphere has a 25 mm $\times$ 18 mm rectangular entrance port that has the same projected area as the SIM prism. This is done to match the diffracted light throughput of this apparatus to the prism. This illumination system produces a 1% total variance in irradiance at the slit plane. The variance was measured by positioning a 1 mm hole in the slit plane and recording the beam intensity. The hole is then moved in 0.5 mm steps to create a raster scan consisting of a grid of beam intensities at 194 locations covering a circular area with a diameter of 13 mm. This intensity map was then used to correct the light intensity when the standard aperture was swapped with the spectrometer slits.

The flux comparison process leads to a measurement equation; terms in this equation are written with subscripts to indicate the standard aperture (aper) and the spectrometer slits (slit):

$$A_{\text{slit}} = A_{\text{aper}} \frac{I_{\text{slit}}}{I_{\text{aper}}} \frac{J_{\text{aper}}}{J_{\text{slit}}} \frac{(1 + 2\alpha_{\text{Cu}}\{T_{\text{M}} - T_{\text{ref}}\})(1 - \beta_{\text{aper}}\lambda)}{(1 + 2\alpha_{\text{slit}}\{T_{\text{M}} - T_{\text{ref}}\})(1 - \beta_{\text{slit}}\lambda)}, \tag{B.3}$$

where $A_{\text{slit,aper}}$: geometric area, for slit and aperture; $I_{\text{slit,aper}}$: measured signal, for slit and aperture; $J_{\text{slit,aper}}$: relative intensity at aperture/slit plane, for slit and aperture; $\alpha_{\text{slit,Cu}}$: coefficient for thermal expansion, 16 and 16.5 ppm $^\circ$C^{-1}, respectively; $T_{\text{M,ref}}$: temperature during measurement and reference temperature (20 $^\circ$C); $\beta_{\text{slit,aper}}$: diffraction correction slope at wavelength λ (11 ppm nm^{-1} for slit, 1 ppm nm^{-1} for aperture).

This measurement is very reproducible with a precision of better than 20 ppm for the selected flight slits. Sixty slits were measured and the slits with the most precise areas and widths were then selected for the flight instrument.

Appendix C

This Appendix is associated with Section 3.3, and describes the Fresnel reflection equations and the apparatus used to deduce the bulk and mirror reflection losses of the Fèry prism.

The Fresnel reflection at the vacuum–glass interface can be characterized in terms of the usual variables (γ, λ, ϕ) presented in Figure 3. Defining two exterior and two interior angles,

$$\gamma_1 = \gamma, \quad \gamma_2 = \gamma - \phi, \quad \beta_1 = \sin^{-1}\left[\frac{\sin\gamma_1}{n}\right], \quad \beta_2 = \sin^{-1}\left[\frac{\sin\gamma_2}{n}\right], \quad \text{(C.1)}$$

from the Fresnel formulas (Jenkins and White, 1976), the transmission for the horizontal and vertical polarizations of light for the two surface transits can be written:

$$\mathcal{T}_{\text{horizontal}} = \left(1 - \left\{\frac{\tan(\gamma_1 - \beta_1)}{\tan(\gamma_1 + \beta_1)}\right\}^2\right)\left(1 - \left\{\frac{\tan(\gamma_2 - \beta_2)}{\tan(\gamma_2 + \beta_2)}\right\}^2\right) \quad \text{and}$$

$$\mathcal{T}_{\text{vertical}} = \left(1 - \left\{\frac{\sin(\gamma_1 - \beta_1)}{\sin(\gamma_1 + \beta_1)}\right\}^2\right)\left(1 - \left\{\frac{\sin(\gamma_2 - \beta_2)}{\sin(\gamma_2 + \beta_2)}\right\}^2\right). \quad \text{(C.2)}$$

The dispersion plane of the prism defines horizontal polarization, and the vertical is defined by the cross-dispersion direction. The average of the two equations in Equation (C.2) would give the transmission of the prism for unpolarized light if it had no bulk losses and the rear surface mirror was a perfect reflector. The light transit from glass-to-vacuum requires some consideration since multiple internal reflections produce a source of scattered light that must be prevented from reaching the detectors. About 5% of the light intensity at this interface is directed towards the base of the prism, where most of the light will escape, but about 4% of this light is internally reflected and then escapes out the apex of the prism. Polishing the base of the prism and coating it with an index refraction matching black epoxy eliminated this problem. Most of the internally reflected light passes through the prism glass and is absorbed by the black coating without reflection (Figure C.1).

The apparatus used to measure prism transmission is schematically shown in Figure 9. A 1000 W xenon arc lamp is used for the source, an ac signal is generated by mechanically chopping the light beam, the bandpass filter is used to limit the wavelength range of light entering the monochromator removing higher orders of light, and a lock-in amplifier is used to determine the light level. The monochromator is set to produce a 0.5 nm resolution light beam for any wavelength over the

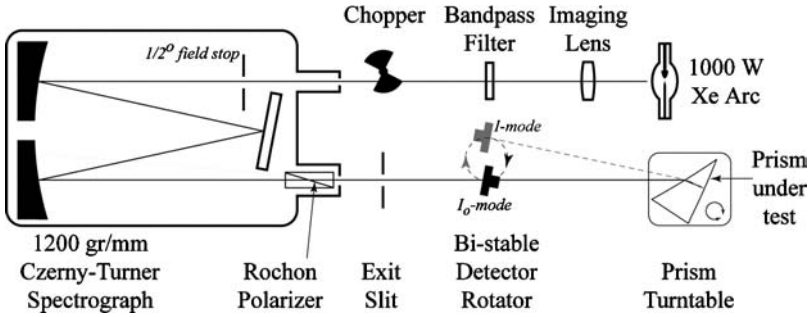

Figure C.1. The apparatus used to determine the transmission of the prism. The measurement is made by ratioing the signal between two rotation positions of the detector (one position shown in *black* and the other in *gray*).

full spectral range of the prism. The MgF_2 Rochon polarizer placed in the output beam is used in two orthogonal orientations, parallel and perpendicular to the long dimension of the exit slit. The calibration is performed in both polarizations to determine the prism transmission after computing and eliminating the contributions from Fresnel reflections. The polarized light exiting the prism is then either detected directly, or after passage through the prism depending on the position of the bi-stable detector rotator. A silicon photodiode is used for visible and UV measurements and a thermoelectrically cooled PbS cell is used for the infrared. A lock-in amplifier operating at the frequency of the light chopper measures the signal from the detectors. The prism is mounted on a precision rotation stage so precise and reproducible rotation angles are achieved. The system is set up to perform the calibration with the ESR's geometry, i.e., the refracted light beam would return to a focus at 35 mm from the entrance slit.

References

Brown, S. W., Eppeldauer, G. P., and Lykke, K. R.: 2000, *Metrologia* **37**, 579.

Edlen, B.: 1953, *J. Opt. Soc. Amer.* **43**, 339.

Fleming, J. C.: 1999, *Reflectivity and BRDF of Nickel-Phosphor Black*, Serial No. S99.41830.OPT.005, Ball Aerospace Corp., Boulder, CO.

Fontenla, J., White, O. R., Fox, P. A., Avrett, E. H., and Kurucz, R. L.: 1999, *Astrophys. J.* **518**, 480.

Fowler, J. B., Saunders, R. D., and Parr, A. C.: 2000, *Metrologia* **37**, 621.

Gere, J. M. and Timoshenko, S. P.: 1990, *Mechanics of Materials*, 3rd edn, PWS-Kent, Boston, Massachusetts, p. 76.

Harder, J. W., Lawrence, G., Fontenla, J., Rottman, G., and Woods, T.: 2005, *Solar Phys.*, this volume.

Humbach, O., Fabian, H., Grzesik, U., Haken, U., and Heitmann, W.: 1996, *J. Non-Cryst. Solids* **203**, 19.

Jenkins, F. A. and White, H. E.: 1976, *Fundamentals of Optics*, McGraw-Hill, New York.

Jorquera, C. R., Korde, R., Ford, V. G., Duval, V. G., and Bruegge, C. J.: 1994, *Geoscience and Remote Sensing Symposium: Proceedings of the IGARSS '94*, 8–12 August, Vol. 4, p. 1998.

Lawrence, G. M., Harder, J., Rottman, G., Woods, T., Richardson, J., and Mount, G.: 1998, *SPIE Proc.* **3427**, 477.
Lawson, C. L. and Hanson, R. J.: 1974, *Solving Least Squares Problems*, Prentice-Hall, Englewood Cliffs, New Jersey, p. 222.
Malitson, I. H.: 1965, *J. Opt. Soc. Amer.* **55**, 1205.
Parr, A. C.: 1996, *A National Measurement System of Radiometry, Photometry, and Pyrometry Based Upon Absolute Detectors*, NIST Technical Note 1421.
Press, W. H., Teukolsky, S. A., Vetterling, W. T., and Flannery, B. P.: 1992, *Numerical Recipes in C: The Art of Scientific Computing*, Cambridge University Press, New York.
Rottman, G., Harder, J., Fontenla, J., Woods, T., White, O., and Lawrence, G.: 2005, *Solar Phys.*, this volume.
Saunders, R. D. and Shumaker, J. B.: 1986, *Appl. Opt.* **25**, 20.
Standish, E. M.: 1982, *Astron. Astrophys.* **114**, 297.
Thuillier, G., Hersé, M., Labs, D., Foujols, T., Peetermans, W., Gillotay, D., Simon, P., and Mandel, H.: 2003, *Solar Phys.* **214**, 1.